Singular Behavior of Slow Dynamics of Single Excitable Cells

Takahiro Harada,[†*] Tomomi Yokogawa,[†] Tomoshige Miyaguchi,[‡] and Hiroshi Kori[§]
[†]Department of Human and Artificial Intelligent Systems, University of Fukui, Fukui, Japan; [‡]Department of Applied Physics, Graduate School of Engineering, Osaka City University, Osaka, Japan; and [§]Division of Advanced Sciences, Ochadai Academic Production, Ochanomizu University, Tokyo, Japan

ABSTRACT In various kinds of cultured cells, it has been reported that the membrane potential exhibits fluctuations with long-term correlations, although the underlying mechanism remains to be elucidated. A cardiac muscle cell culture serves as an excellent experimental system to investigate this phenomenon because timings of excitations can be determined over an extended time period in a noninvasive manner through visualization of contractions, although the properties of beat-timing fluctuations of cardiac muscle cells at the single-cell level remains to be fully clarified. In this article, we report on our investigation of spontaneous contractions of cultured rat cardiac muscle cells at the single-cell level. It was found that single cells exhibit several typical temporal patterns of contractions and spontaneous transitions among them. Detrended fluctuation analysis on the time series of interbeat intervals revealed the presence of $1/f^{\beta}$ noise at sufficiently large timescales. Furthermore, multifractality was also found in the time series of interbeat intervals. These experimental trends were successfully explained using a simple mathematical model, incorporating correlated noise into ionic currents. From these findings, it was established that singular fluctuations accompanying $1/f^{\beta}$ noise and multifractality are intrinsic properties of single cardiac muscle cells.

INTRODUCTION

Power-law correlated fluctuations with long-term correlations are known to present in various types of physiological signals, and characteristics of these fluctuations provide important information on the internal state of an organism (1,2). Such fluctuations are found in complex systems in which many regulatory mechanisms interact, including the cardiovascular system (1,3,4), the auditory nervous system (5), and the motion control system (6,7). It is thus supposed that interactions between multiple regulatory systems are essential to generate the abovementioned fluctuations. In contrast, it has also been established that isolated cells exhibit power-law correlated fluctuations at large timescales without extrinsic control systems. Examples include spontaneous contractions of cardiac muscle cells (8–11), and membrane currents associated with exocytosis in nerve cells and fibroblasts (12). Because this phenomenon has been observed in multiple cell types, power-law correlated fluctuations at large timescales might be a generic property over various types of cells. However, little of the mechanism underlying the generation of such fluctuations has been established so far.

A cardiac muscle cell culture is an excellent model system for studying the characteristics of power-law correlated fluctuations. This is because of several unique properties of cultured cardiac muscle cells. Firstly, the timing of electric excitations of a cell can be estimated by visualizing its contraction, because a depolarization of the membrane potential is associated with a contraction of muscle fibrils in a well-established manner (13). This enables us to perform long-term noninvasive measurement of excitation timings (14,15). Secondly, one can continuously measure the activity of a cell without the measurement being disrupted by the cell cycle, because these cells are terminally differentiated. Thirdly, the molecular mechanism of excitation-contraction coupling has been extensively investigated in past studies, and considerable knowledge about this process has been accumulated (16).

For cultured cardiac muscle cells, the existence of power-law correlated fluctuations in the spontaneous beat rate has been reported in earlier studies (9–11). However, because the former studies were mainly performed on a monolayer culture in which a number of cells interacted with each other through a gap junction, the characteristics of isolated single cells are not fully understood. In particular, it is not clear whether $1/f^{\beta}$ noise and multifractality, both of which have been identified in the interbeat interval time series of the human heartbeat (3,17,18), are also intrinsic properties of single cardiac muscle cells.

To clarify the origin of the power-law correlated fluctuations and to provide a basis for further studies of fluctuations observed at higher levels of organization, i.e., in tissues, organs, and organ systems, it is of fundamental importance to clarify the properties of single cells that have no physical and electric interactions with other cells. In this study, we examined the statistical properties of the spontaneous beat timings of single cardiac muscle cells derived from neonatal rat ventricles over an extended timescale. As a consequence, we were able to make the following observations.

Firstly, several typical temporal patterns were identified in the spontaneous contractions of isolated single cardiac muscle cells. These patterns included steady beating, termed pattern *A*, and intermittent bursts, termed pattern *B*. Under the same environmental conditions, the temporal pattern of contractions differs from cell to cell. Furthermore, spontaneous transitions

Submitted June 9, 2008, and accepted for publication September 16, 2008.

*Correspondence: harada@life.ne.his.fukui-u.ac.jp

Editor: Michael D. Stern.

0006-3495/09/01/0255/13 $2.00

doi: 10.1529/biophysj.108.139691

between patterns were found in the same single cell during a long-term observation. We studied the statistical properties of the above-mentioned temporal patterns. For pattern *A*, the distribution of interbeat intervals (IBIs) formed a γ-like unimodal distribution. $1/f^{\beta}$ noise ($\beta \approx 1$) was identified in the IBI time series at sufficiently large timescales. As for pattern *B*, the IBIs followed a bimodal distribution. $1/f^{\beta}$ noise was also identified in the IBI time series of pattern *B* at sufficiently large timescales. Furthermore, both patterns possessed multifractality, i.e., the local Hölder exponents possessed a broad spectrum exhibiting a peak at ~0. These experimental trends were successfully explained by an integrate-and-fire-type mathematical model, which was originally described by Izhikevich (19), in which we additionally incorporated a long-term-correlated noise. These findings strongly suggest that $1/f^{\beta}$ noise and multifractality in IBI time series are intrinsic properties of isolated single cardiac muscle cells.

METHODS

Preparation of cell culture

The experimental procedures were approved by the Animal Use and Care Committee of the University of Fukui (Fukui, Japan). Primary cultures of ventricular cells were prepared from one-day-old neonatal rats according to methods described elsewhere (20,21). Briefly, ventricles isolated from hearts of one-day-old rats were minced and were treated with collagenase (0.2% dissolved in phosphate-buffered saline) at 37°C for 10 min. The treatment was repeated four times, and the supernatant from the second to the fourth treatments were collected. The selective plating method (22) was adopted to reduce the population of nonmuscle cells; the cells were supplied with plating medium (90% Dulbecco-modified Eagle medium, 10% fatal bovine serum, 0.1 mM 5-bromo-2′-deoxyuridine (BrdU) and 1% penicillin/streptomycin solution) and plated on a petri dish. After a 90-min incubation at 37°C and 5% CO_2, the supernatant was collected. Cells were further purified by Percoll-density-gradient centrifugation (22); the cells were dispersed in a suspension buffer (116 mM NaCl, 20 mM 4-(2-hydroxyethyl)-1-piperazineethanesulfonic acid (HEPES), 1 mM NaH_2PO_4, 5.5 mM D-glucose, 5.4 mM KCL, and 0.8 mM $MgSO_4$) and were overlaid on a Percoll suspension forming a discontinuous density gradient (35% and 45%). Thirty-minute centrifugation at 3000 rpm resulted in the formation of a band between 35% and 45% Percoll suspension. The cells were collected and again suspended in a plating medium to achieve a density of 1.3×10^4 cell/ml. Two milliliters of cell suspension were plated on a type-I-collagen-coated ϕ 35-mm petri dish. After 24-h incubation at 37°C and 5% CO_2, the medium was replaced with a contraction medium (90% modified Eagle medium, 10% calf serum, 0.1 mM BrdU, 1% penicillin-streptomycin solution). This was followed by incubation at 37°C and 5% CO_2 for 1–3 days.

Measurement of spontaneous beating activity

Cells cultivated for 2–4 days were used in the measurement of spontaneous activity. First, the medium in a culture dish was exchanged with a fresh contraction medium (see above for the composition of the medium). It was then placed on a homemade on-stage cultivating chamber mounted on an inverted phase-contrast microscope (IMT-2, Olympus, Tokyo, Japan). The interior of this cultivating chamber was maintained at 37 ± 0.5°C, 5% CO_2, and in a humidified condition. By using this chamber, we were able to keep the isolated cells vital for several days. In this study, to avoid the possible effect of medium exchange, the medium was not exchanged during the measurement, and the duration of a single measurement did not exceed 12 h. Although a small fraction of nonmuscle cells contaminated the primary culture, we were able to identify vital muscle cells with ease because they exhibited spontaneous contractions. We chose ~10 isolated cells at random in a single field of view of the microscope, whose size was ~900 × 680 μm^2. Although many cells were isolated, in some cases, a few cells were clustered, forming a small aggregate. The phase-contrast microscopic images of cells were obtained via a 4 × objective lens and a charge-coupled-device camera (WAT-902H2, Watec, Yamagata, Japan) at a frame rate of 30 frames/s. The data were continuously stored on a hard-disk drive for later analysis.

Data processing

Detection of spontaneous contractions

The timings of spontaneous contractions were determined from a sequence of the phase-contrast microscopic images (30 frames/s). Contractions of a cell are associated with a sequential change in the brightness of pixels, in particular those located near the cellular boundary (Fig. 1 *a*). The pixel that exhibited the largest frequency of sufficiently large peaks in the time series of brightness was then automatically selected, and the time series of the brightness associated with this pixel was analyzed. To remove slow modulation of a baseline of brightness, the local averages of brightness calculated for each 10 s were subtracted from the original data. Furthermore, a moving-average filter over three or five frames was applied to reduce shot noise in the time series (Fig. 1 *a*). The positions of the peaks whose maximal values exceeded a prescribed threshold were associated with the timings of contractions.

Next, to remove fictitious spikes due to shot noise that were not removed by the filtering we have discussed, spikes whose interval from the preceding spike was less than a prescribed threshold value were removed (Fig. 1 *a*). This threshold was determined as follows. First, a histogram of IBIs was constructed, which usually had a peak ~1 s. Second, a secondary peak sometimes appeared at a much smaller interval (typically <0.2 s). These IBIs are due to the shot noise mentioned above, as exemplified in Fig. 1 *a*. Third, the threshold value was set to the value of IBI that gave a minimum between these two peaks. The value of the threshold was typically <0.3 s (the average was 0.2 s). This procedure resulted in the removal of 8.8% of spikes on average. Afterwards, by inspection of the profile of the fluctuation function in the detrended fluctuation analysis, it was confirmed that this spike removal had a negligible effect on the long-term behavior of the IBI time series, including the scaling exponent, α, of large timescales in the detrended fluctuation analysis.

By accounting for the drift of the microscope stage and a slight gradual deformation of the cell, the position of the analyzed pixel and the threshold value for peak detection were updated every 1200 s. The above-mentioned semiautomatic method of spike detection enabled us to reduce the probability of misdetection of spikes down to 0.5%, compared to the case where spikes were fully manually identified. In the following, statistical data are represented as mean ± SE, if not otherwise indicated.

Construction of a contraction-time map

Spatial distribution of the timings of contraction was determined as follows. First, contraction events were detected for each cell or small cluster using the same method as described above. Second, the time difference of the sequence of phase-contrast images was calculated. In this analysis, the length of the time series was set to 1000 frames ($\approx$33.3 s) for every cell. Around the timing of every contraction event, a peak was identified for each pixel in the time-difference images. In this process, to remove the effect of measurement noise, peaks whose absolute value was less than a certain threshold were eliminated. The value of the threshold was manually determined. If multiple peaks were found around a single contraction event, the preceding peak was selected because the earlier one corresponds to the timing of contraction and the later one corresponds to the timing of relaxation. Third, the time delays of the peaks in each pixel from the earliest peak in the cell were calculated for every contraction event. The delay values were averaged over

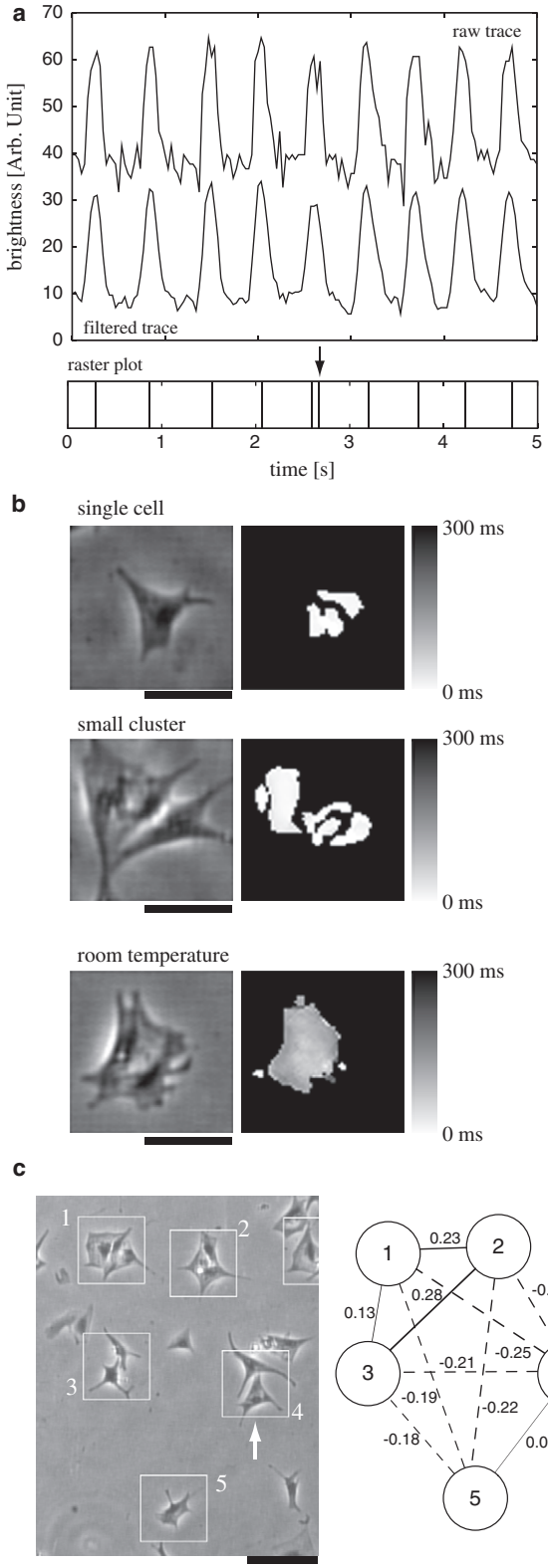

FIGURE 1 (*a*) An example of a trace of brightness of a pixel on the cell indicated by the arrow in panel *c*. The upper trace in the upper panel represents raw data. The lower trace represents filtered data, which was generated by taking a moving average over three video frames. The value of brightness is expressed at the eight-bit resolution, and the baselines of the traces are arbitrarily shifted so that they can be seen easier. The lower panel represents a raster plot constructed from the filtered data. Each vertical line indicates the occurrence of a beat. In a raster plot, fictitious spikes were sometimes generated due to noise in the raw trace. An example of these fictitious spikes is indicated by an arrow above the raster plot. These fictitious spikes were identified by the procedure described in the text and were removed. (*b*) Contraction-time map. The left panels exemplify phase-contrast images of cells. The scale bar represents 50 μm. In the right panel, a map of the delay in the timings of contraction (sharp changes in the brightness) from the earliest timing in each contraction, averaged over 1000 frames (~30 contractions), was represented. The gray level represents the magnitude of delay as indicated in the right bar. The top row displays an example of a map for an isolated single cell. The middle row exemplifies the case of a small cluster. In these cases, the delays were typically within one frame (33 ms). The average of delays over 25 cells was 0.44 $\pm$ 0.11 frames. For comparison, the contraction-time map for a small cluster at 27°C in the absence of bicarbonate buffer system, which displays propagation of contraction waves within a cell, is shown at the bottom. In this case, significant delays were observed. (*c*) (*Left*) A phase-contrast image of several cardiac muscle cells in the same field of view. The solid boxes indicate the cells whose spontaneous contractions have been analyzed. The scale bar represents 100 μm. (*Right*) Pairwise correlations of the time series of beat rates for five cells shown in the left panel. Each circle with a number corresponds to the same-numbered cell in the left panel. A line connecting two circles represents the correlation coefficient, r, of the beat rate; the thickness of the line is proportional to the magnitude of r, and the solid and dashed lines mean positive and negative signs for r, respectively. The value of r is also indicated on each line. The average of r for these five cells was -0.055 ± 0.066.

the entire set of contraction events for each pixel on the cell. Fourth, the map of the averaged delays was constructed by expressing their values using a grayscale (see Fig. 1 *b*).

Detrended fluctuation analysis (DFA)

In this study, we used detrended fluctuation analysis (DFA) (23), which is a widely utilized method for analysis of autocorrelation of nonstationary time series, to examine the autocorrelation inherent in the time series of IBIs. First, letting x_i be the IBI between the ith and $(i + 1)$th beats, we constructed an integrated IBI time series, $y_i = \sum_{j=1}^{i} x_j$. The integrated IBI time series was divided into bins of size n. In the jth bin, a linear local trend, $\{\bar{y}_i^j\}$, which was determined by least-squares fitting, was subtracted from the original time series. The root mean-square of the deviations from local trends, represented by

$$F(n) \equiv \sqrt{\frac{1}{mn}\sum_{j=1}^{m}\sum_{i=jn+1}^{(j+1)n}\left(y_i - \bar{y}_i^j\right)^2}, \qquad (1)$$

depends on the bin size, n, and is termed a fluctuation function. In the above expression, m represents the number of bins of size n, and $\{\bar{y}_i^j\}$ represents the linear local trend in the jth bin. If the original IBI time series, $\{x_i\}$, possesses scale-invariance, the fluctuation function, $F(n)$, will exhibit a scaling of the form $F(n) \simeq n^{\alpha}$. The scaling exponent, α, is related to the scaling exponent, β, of the power spectrum density of the original IBI time series, assuming the form $S(f) \simeq f^{-\beta}$, as $2\alpha = \beta + 1$.

Multifractal analysis

To assess the multifractality in the IBI time series, we adopted the wavelet-transform modulus-maxima (WTMM) method, originally proposed by Muzy et al. (24). Let us describe this method briefly; the local Hölder exponent, h_i, is a quantity locally characterizing the deviation of the IBI time series, $\{x_i\}$, as

$$|x_i - x_{i+1}| \simeq l^{h_i}. \qquad (2)$$

Let $D(h)$ represent the Hausdorff dimension of the subset where the local Hölder exponent coincides with h. According to Muzy et al. (24), $D(h)$ can be determined as follows. First, the integrated IBI time series $\{y_i\}$ was trimmed to a size of $N = 2^{14}$ or 2^{15}, depending on the length of the original time series. The time series was then discrete-wavelet-transformed using a fast Fourier transform as

$$T_i(s) \equiv \frac{1}{s}\sum_{j=1}^{N} y_j \psi\left(\frac{i-j}{s}\right). \quad (3)$$

The fourth derivative of a Gaussian function, $\psi(t)$, was adopted as an analyzing wavelet. With this choice of analyzing wavelet, we were able to remove up to third-order polynomial trends in the time series (24).

Next, the wavelet coefficient $T_i(s)$ was linearly interpolated at three intermediate points for each i. Letting the interpolated time series be denoted by $\tilde{T}_i(s)$ ($i = 1, 2, \cdots, 4N$), modulus-maxima curves were determined from maxima of $|\tilde{T}_i(s)|$ with respect to i for every s. Let $\mathrm{L}(s_0)$ express the set of modulus-maxima curves, ℓ, satisfying $(i, s) \in \ell \Rightarrow s \leq s_0$, and $\forall s < s_0$, $\exists (i, s) \in \ell$. Using this notation, a partition function can be defined as

$$Z_q(s) \equiv \sum_{\ell \in \mathrm{L}(s)} \left[\sup_{(i,s') \in \ell} |\tilde{T}_i(s')| \right]^q. \quad (4)$$

Then, if the time series possess scale-invariance, the partition function, $Z_q(s)$, behaves like

$$Z_q(s) \simeq s^{\tau_I(q)}. \quad (5)$$

In this article, we utilize the integrated IBI time series, $\{y_i\}$, for analysis, for the sake of numerical stability. The scaling exponent, $\tau(q)$, of the partition function for the original time series, $\{x_i\}$, is determined from the exponent, $\tau_I(q)$, for the integrated time series using the relation

$$\tau(q) = \tau_I(q) - q. \quad (6)$$

The value of $\tau(q)$ has a simple physical meaning in some special cases. In particular, $\tau(2)$ is related to the scaling exponent of the power spectrum density, β, as $\beta = \tau(2) + 2$. The spectrum of the local Hölder exponents for the original time series is obtained by the Legendre transform of $\tau(q)$ as

$$D(h) = qh - \tau(q). \quad (7)$$

Numerical simulation

We adopted the Euler method for numerical simulations of the mathematical model. The size of the time step, Δt, was set to 0.05. The timing of firings, i.e., the timings at which the excitation variable exceeded a threshold, were determined by interpolating the orbit obtained using the finite time step Δt, by extending the method used in Hansel et al. (25).

RESULTS

Spontaneous activity of single cells

Ventricular muscle cells derived from neonatal rats were plated on a collagen-coated petri dish at a low density. After one day from the onset of cultivation, the cells were found to adhere to the substratum and to exhibit spontaneous contractions. At a cellular density of ~30 cells/mm^2, which was adopted in this study, many cells were physically isolated although in some cases cells occasionally coupled to form a small cluster of cells, as can be seen in Fig. 1 *c*. In the digital images obtained through phase-contrast video microscopy, pixels on these cells exhibit cyclic changes of brightness as exemplified in Fig. 1 *a*. The timings of spontaneous contractions can be estimated from the time series of brightness for each pixel.

In this experimental setup, in which pH of the culture medium was regulated by a bicarbonate buffer system and the temperature was kept at 37°C, the timing of every contraction was almost simultaneous either within single cells or small clusters of cells, as depicted in Fig. 1 *b* (the mean delay was 0.44 ± 0.11 video frames). This was a clear contrast to the case where the cells were left at the room temperature and pH of the medium was controlled by HEPES buffer (pH 7.3). In this case, slow propagation of contraction was frequently observed within a single cell (see the *bottom panels* in Fig. 1 *b*). This is considered as a manifestation of Ca^{2+} waves, because the velocity of propagation of contraction is consistent with the velocity of a Ca^{2+} wave, which is ~100 μm/s (26). In contrast, in our experimental setup, a propagation of contraction occurs within one video frame for a cell whose diameter is ~100 μm. This is therefore too fast to be explained by Ca^{2+} waves. This finding led us to conclude that every contraction is accompanied by an action potential in our experimental setup.

In addition, it was confirmed through this analysis that wave propagation is absent even for small clusters consisting of a few cells. We thus assumed that network effects are absent for small clusters in this study (confirmed later), and, in the following, we analyzed spontaneous contractions of isolated single cells and small clusters containing up to three or four cells by regarding them as a single unit. The following analysis involves 23 isolated single cells, 18 clusters consisting of two cells, four clusters consisting of three cells, and two clusters consisting of four cells. As mentioned later, significant difference was not observed in the statistical properties of spontaneous contractions for different sizes of clusters.

As for pairs of cells distant from each other, in contrast, correlations in the activity of spontaneous contractions were not observed. As depicted in Fig. 1 *c*, consistent correlations were not observed in the beat rates among distant cells in the same field of view. The absolute value of the average of correlation coefficients of the beat rate was <0.1. This finding indicates that fluctuations in the beat timings were dominantly generated by fluctuations of the internal states of the cells, rather than fluctuations of environmental conditions such as temperature and pH.

In the spontaneous contractions of isolated cardiac muscle cells, several typical temporal patterns were identified. First, a state in which steady contractions continued over several hours was often observed. This pattern was termed pattern *A*. An example of this pattern is displayed in Fig. 2 *a* as a raster plot. In another case, alternate occurrences of burst phases and quiescent periods were also often observed. This pattern, termed pattern *B*, is depicted in Fig. 2 *b*. Each burst phase typically involves several tens of beats with IBIs at ~1.0 s. The duration of a quiescent

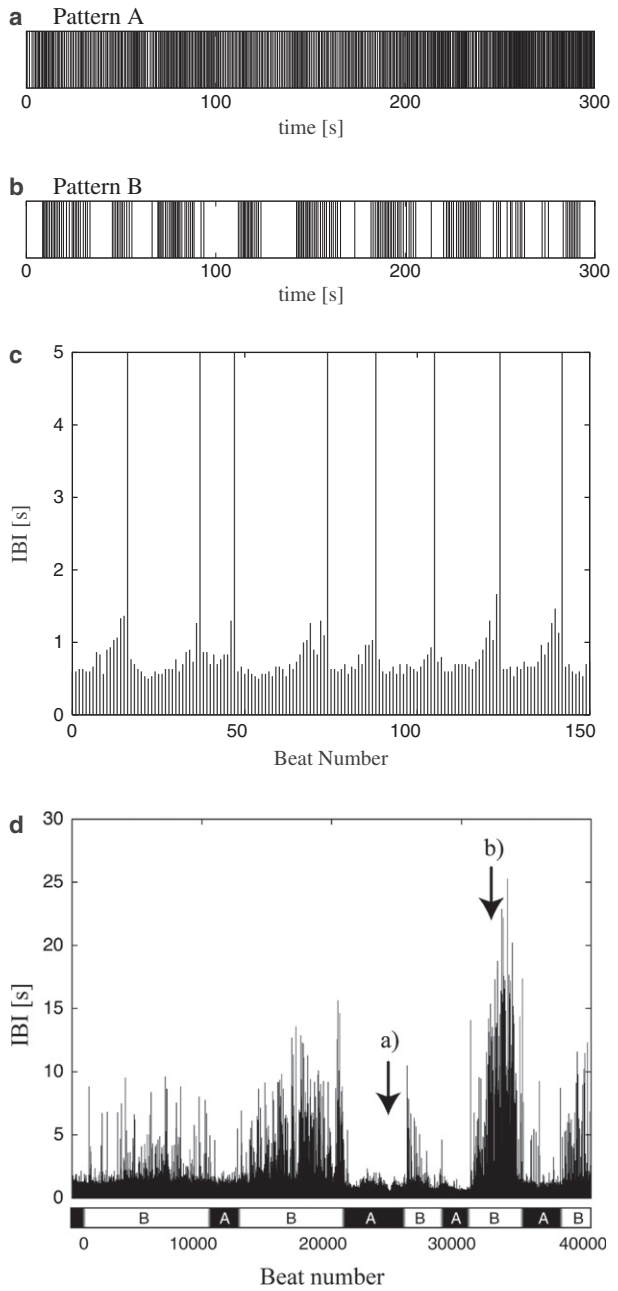

FIGURE 2 Typical temporal patterns in the spontaneous contractions of single cardiac cells. (*a*) Raster plot of a segment of pattern *A*: beats occur with relatively regular timings. (*b*) Raster plot of a segment of pattern *B*: an intermittent burst pattern. Bursts, each involving several tens of beats, are separated by quiescent periods of several tens of seconds. (*c*) The time series of the interbeat intervals (IBIs) in pattern *B*. Vertical lines are drawn to emphasize very long IBIs (quiescent periods); the eight long vertical lines in the figure correspond to quiescent periods, which are longer than 5 s. The IBIs become gradually longer in advance of the occurrence of a quiescent period (type I burst). (*d*) An example of spontaneous transitions between patterns. The time series of IBIs are displayed for an extended duration. On the bottom of the plot, the annotations of the patterns associated with each part of the IBI time series are represented. The raster plots presented in panels *a* and *b* were constructed from the portion of the time series marked by arrows.

period typically ranges from several seconds to several tens of seconds. As displayed in Fig. 2 *c*, it was sometimes observed that IBIs became gradually larger before an incidence of a quiescent period. This observation implies that the burst behavior found here can be classified as bursts of Type I (27). Although similar bursting activity was observed in a network of cultured cardiac muscle cells in earlier studies (28,29), this was caused by spontaneous initiation and annihilation of rotating waves. By contrast, since network effect is absent in our experimental setup as discussed above, the bursting activity observed here should has a different origin from those observed in a network of cells.

Although the experimental conditions were the same for all cells, the observed patterns varied from cell to cell. Furthermore, in some cases, spontaneous transitions from one pattern to the other were observed over a long experimental period, as exemplified in Fig. 2 *d*. This observation implies the presence of a slowly fluctuating variable controlling the appearance of patterns and involved in the mechanism that determines the temporal patterns of spontaneous contractions.

Statistical properties of interbeat intervals

To characterize the statistical properties of beat timings, variation over time of beat rates, probability distribution of IBIs, and autocorrelation of the time series of IBIs, were examined for every contraction pattern. First, in the time series of beat rates, i.e., the numbers of beats in 1 min, rapid fluctuations were superimposed on slow modulations for both patterns (see Fig. 3, *c* and *d*). The magnitude of the rapid fluctuations was larger in pattern *B*. As depicted in Fig. 3 *e*, the histogram of IBIs for pattern *A* exhibits a γ-like unimodal distribution whose peak was located at ~1 s. In contrast, for pattern *B*, the histogram of IBIs typically possesses two peaks, one peak at <1 s and the other at several tens of seconds. In some cases, a fat tail appears instead of the second peak for large IBIs.

Next, to study the autocorrelation of the time series of IBIs, we performed a detrended fluctuation analysis (DFA) (23). Fig. 3, *g* and *h*, displays the fluctuation function, $F(n)$, calculated for patterns *A* and *B*, respectively. As seen in these plots, $F(n)$ is found to be a monotonically increasing function of bin size, n. From Fig. 3 *g*, two scaling regions were identified for pattern *A*. In the scaling region for small n ($n < 10^2$), the scaling exponent α was ~0.5, indicating that the fluctuations of beat timings are uncorrelated for short timescales. In the scaling region for large n ($n > 10^{2.5}$), the slope of the $F(n)$ in the logarithmic plot significantly deviates from 0.5, and the scaling exponent in this region was close to unity (for the example displayed in Fig. 3 *g*, $\alpha = 0.89 \pm 0.03$). As for pattern *B*, three distinct scaling regions were identified, in contrast to the case of pattern *A*. First, pattern *B* also exhibits a scaling region for small n, where the

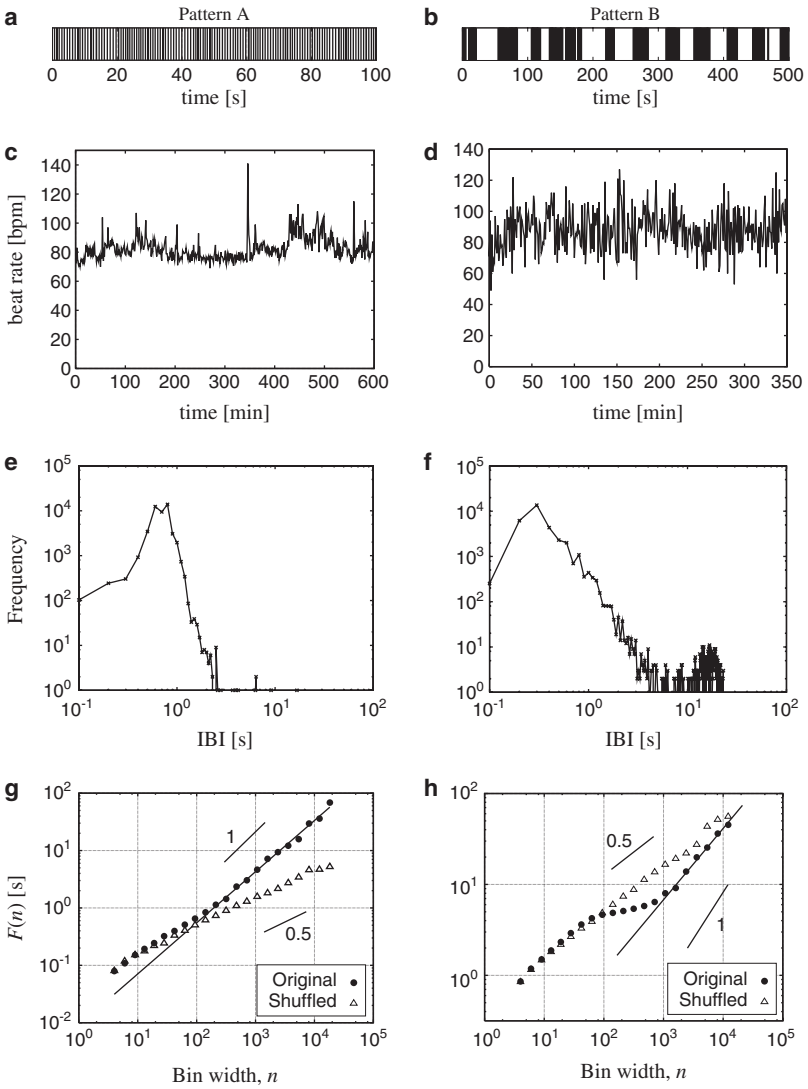

FIGURE 3 Statistical properties of the IBI time series of patterns *A* and *B*. The left columns (*a*, *c*, *e*, and *g*) represent data for pattern *A*, and the right columns (*b*, *d*, *f*, and *h*) display data for pattern *B*. Data for typical cells are displayed. (*a* and *b*) Raster plots of a portion of the time series for pattern *A* and pattern *B*. (*c* and *d*) Time series of the beat rate, represented as the number of beats per minute. (*e* and *f*) Histograms of the IBIs. (*g* and *h*) Detrended fluctuation analysis (DFA). The fluctuation function for the detrended IBI time series, $F(n)$, is plotted as a function of the bin size for detrending, n, in a logarithmic plot. The solid circles represent data constructed from the original IBI time series. The open triangles represent data constructed from randomly shuffled IBI time series. The solid lines are the least-squares fits to the original data in the range $[10^{2.5}, 10^{4.5}]$ in *g* and $[10^{3.2}, 10^{4.5}]$ in *h*, respectively. The scaling exponents α in these regions are 0.89 ± 0.03 in *g* and 0.78 ± 0.03 in *h*, respectively.

exponent was ~0.5. In the case of pattern *B*, the fluctuation function, $F(n)$, exhibits a plateau in the intermediate scale ($10^2 < n < 10^3$). For larger n, $F(n)$ exhibits a scaling exponent $>>0.5$ (in Fig. 3 *h*, $\alpha = 0.78 \pm 0.03$), as was the case for pattern *A*.

Fig. 4 *a* displays a histogram of the scaling exponents of $F(n)$ for each cell in the scaling region for large n. Because classification of the patterns is not clear in some cases, the histogram is represented with both patterns unified. As clearly observed in this figure, the scaling exponent, α, has a distribution with a peak at ~0.9. The value of the scaling exponent, α, averaged over all the cells analyzed here ($n = 47$) yielded the value 0.91 ± 0.03. Averaging over pattern *A* ($n = 29$) gives the value 0.93 ± 0.03, and averaging over pattern *B* ($n = 18$) yields the value 0.87 ± 0.04.

The number of coupled cells has no effect on the scaling exponent, α. Fig. 4 *b* displays the exponent α averaged over clusters that contain the specified number of cells. As seen in this figure, no significant variation in the value of α was observed for different sizes of clusters ($p = 0.83$, one-way ANOVA test).

From the above observations, it became clear that the fluctuations of beat timings of single cells possessed a long-term correlation, and can be characterized as $1/f^{\beta}$ noise, with $\beta \approx 1$, at timescales larger than 10^3 events.

Multifractality

Next, we performed multifractal analysis to gain further information about the correlation of IBIs. Multifractality is a concept developed to characterize geometrical objects where the scaling exponent of its measure is not unique but has a spectrum (24,30,31). Time series can also possess multifractality. In particular, the time series of IBIs in the heart rate of a healthy young human is a well-known example of a time series possessing multifractality (18,32). Here, to assess multifractality in the time series of IBIs for single cells, we adopted the wavelet-transform modulus-maxima (WTMM) method, presented by Muzy et al. (24,31). Fig. 5

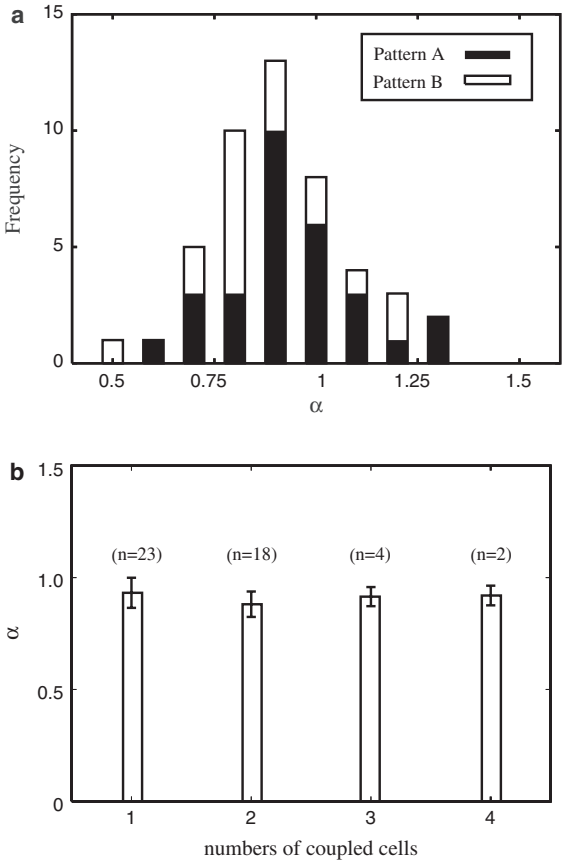

FIGURE 4 (*a*) The histogram of exponent α in the scaling region of large timescales in DFA. The solid bars represent numbers of cells exhibiting pattern *A*, and the open bars represent numbers of cells exhibiting pattern *B*, possessing the specified value of α. (*b*) The relation between the number of coupled cells and the exponent, α. The horizontal axis represents the number of cells in a single cluster. The vertical axis represents the average of the exponent, α, in the scaling region of large timescales in DFA. The number of samples is indicated on the top of each bar. Note that there is no significant difference in the value of α over different sizes of clusters.

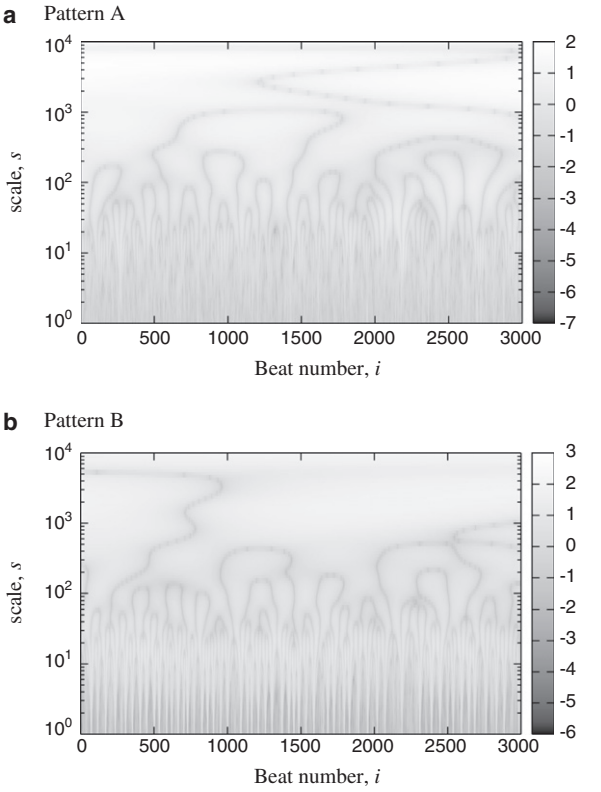

FIGURE 5 Wavelet transform of integrated IBI time series. Small portions of the entire time series are presented. The horizontal axes represent the number of beats, *i*, and the vertical axes represent the wavelet scales, *s*. The gray levels represent the logarithm of the absolute value of the wavelet coefficient, $\log_{10}|T_i(s)|$. (*a* and *b*) Display examples from pattern *A* and pattern *B*, respectively.

exemplifies the wavelet coefficients of the integrated IBI time series, $\{y_i\}$, for pattern *A* and *B*. In this study, we adopted the fourth derivative of a Gaussian function as an analyzing wavelet. According to Muzy et al. (24), this allows us to remove polynomial trends with orders less than four. This figure graphically demonstrates the fractal nature of the time series of IBIs.

Fig. 6, *a* and *b*, display the partition functions, $Z_q(s)$, which are calculated according to Eq. 4, for the same cells displayed in Fig. 5, *a* and *b*, respectively. This figure shows that the profile of the partition function varies as the value of q changes. Similarly to the case of DFA (see Fig. 3 *g*), two scaling regions were found in the partition function for pattern *A*, one for small scales ($s < 10^2$) and the other for large scales ($s > 10^2$). As for pattern *B*, three scaling regions, one for small scales ($s < 10^{1.5}$), one for intermediate scales ($10^{1.5} < s < 10^{2.5}$), and the third for large scales ($s > 10^{2.5}$), were identified in the profiles of partition functions, as occurred with DFA (see Fig. 3 *h*).

Because we are interested in the property of the time series for the large scales, we determined the scaling exponents in the region $[10^{2.5}, 10^4]$, by least-squares fitting of the logarithmic plots of the partition functions to linear functions. From these exponents, through the conversion given by Eq. 6, the spectra of $\tau(q)$ were obtained (Fig. 6, *c* and *d*). As observed in the figure, the spectra of $\tau(q)$ deviate from straight lines for both patterns *A* and *B*, implying the presence of multifractality. This finding also suggests that the time series of IBIs are nonuniform, and that the local Hölder exponent h in the time series is not unique. The spectrum of the local Hölder exponents, $D(h)$, can be obtained by the Legendre transform of $\tau(q)$. Fig. 6, *e* and *f*, displays the spectra, $D(h)$, for patterns *A* and *B*, respectively. From these plots, it is obvious that the local Hölder exponent, h, possesses a broad spectrum. In the case exemplified in Fig. 6, *e* and *f*, the spectra, $D(h)$, exhibit maxima at $h = -0.04$ and $h = -0.15$ for patterns *A* and *B*, respectively. The fact that the local Hölder exponents exhibit a maximum at $\sim h = h_{\max} \approx 0$ provides an independent confirmation of the result of DFA, confirming the presence of $1/f^{\beta}$ noise in the time series of IBIs. The maximal

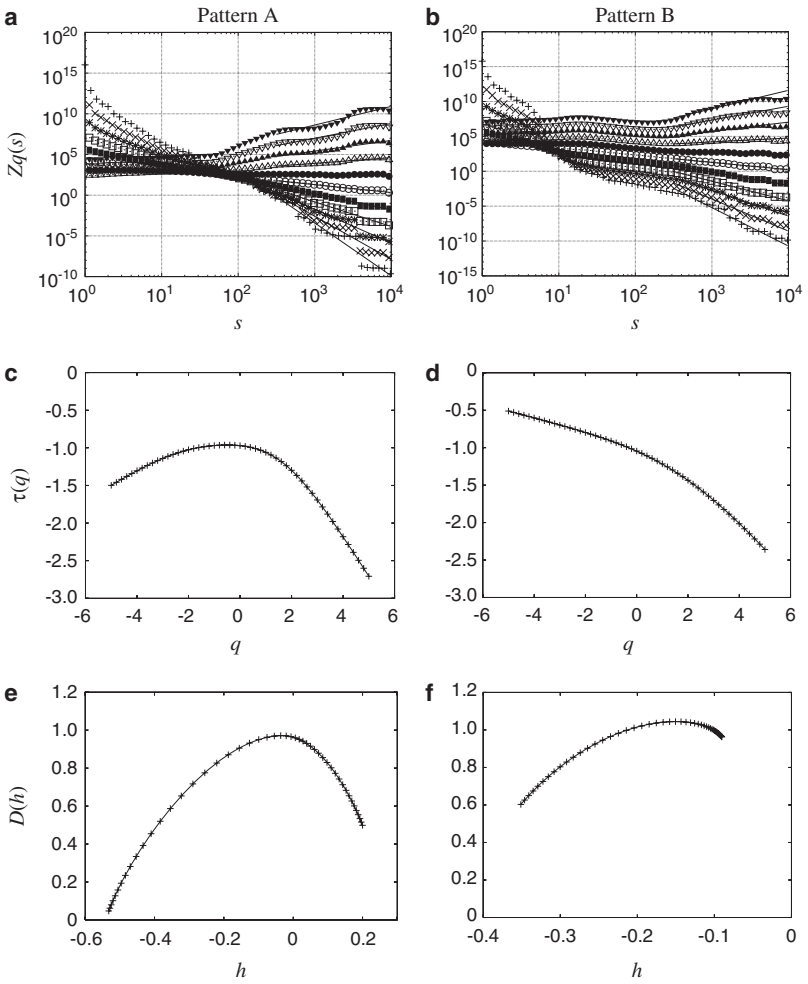

FIGURE 6 Multifractal analysis of the IBI time series. The left columns (*a*, *c*, and *e*) represent data for pattern *A*, and the right columns (*b*, *d*, and *f*) display data for pattern *B*. (*a* and *b*) Partition functions, $Z_q(s)$, of integrated IBI time series. $Z_q(s)$ for several values of q are represented as functions of wavelet scales in logarithmic plots. Vertical crosses, tilted crosses, asterisks, open squares, solid squares, open circles, solid circles, open upward triangles, solid upward triangles, open downward triangles, and solid downward triangles represent the partition functions for $q = -5, -4, -3, -2, -1, 0, 1, 2, 3, 4$, and 5, respectively. Thin solid lines are the least-squares fits to the data in the range $[10^{2.5}, 10^4]$. (*c* and *d*) The spectrum of the scaling exponent, $\tau(q)$, for the original IBI time series. (*e* and *f*) The spectrum of the local Hölder exponents, $D(h)$, for the original IBI time series.

value, $D(h_{\max})$, was approximately unity, indicating that the time series were almost everywhere singular. These features were consistently observed in most of the cells analyzed here ($n = 13$: eight cells with pattern *A*, five cells with pattern *B*). However, the value of $h_{\max}$ was different from cell to cell, ranging from -0.30 to 0.17. The average was -0.033 ± 0.043. In addition, the range of h for the spectrum of $D(h)$, denoted by R_h, also varied from cell to cell, ranging from 0.06 to 0.84. The average was 0.41 ± 0.07. No significant correlation has been found in the multifractal properties, including the values of $h_{\max}$ and R_h, and the number of cells in a single cluster ($p = 0.60$ for $h_{\max}$ and $p = 0.56$ for R_h, one-way ANOVA test).

Model

We next analyzed experimental data by constructing a simple mathematical model. The outstanding feature observed in the behavior of single cells is the presence of several characteristic temporal patterns (*A* and *B*). In particular, the characteristic of a type-I burst (27) was found in pattern *B*, as depicted in Fig. 2 *c*. We thus adopted an integrate-and-fire model originally proposed by Izhikevich (19) in this study, because this is the simplest model that exhibits a type-I burst. Although the originally proposed model is deterministic, we added white Gaussian noise to the dynamics of an excitation variable, which could represent the membrane potential, because thermal noise is expected to contribute to ionic currents at the single-cell level. We further added another noise component with a long-term correlation to the ionic currents, by assuming that this component reflects an internal state of the cell. Since no network effect was observed in the experiment, spatial degrees of freedom are not considered here. By including these modifications, we prepared the model as follows. First, the continuous dynamics are described as

$$\tau\dot{x} = I + x^2 - y + z + \xi, \tag{8}$$

$$\tau\dot{y} = -\mu y, \tag{9}$$

where $x(t)$ and $y(t)$ represent an excitation variable and a slow recovery variable, respectively. In addition, when $x(t)$ reaches a prescribed threshold x_{th}, $x(t)$ is reset and $y(t)$ is increased as

$$x \rightarrow 1, \tag{10}$$

$$y \rightarrow y + d. \tag{11}$$

The term $\xi(t)$ that occurs in Eq. 8 is white Gaussian noise satisfying $\langle \xi(t) \rangle = 0$ and $\langle \xi(t)\xi(0) \rangle = 2D\delta(t)$. The term $z(t)$ is long-term correlated Gaussian noise, constructed as

$$z(t) \equiv \frac{1}{\sqrt{N_z}} \sum_{i=1}^{N_z} z_i(t), \tag{12}$$

$$\dot{z}_i = -k_i z_i + \zeta_i \quad \text{for} \quad i = 1, 2, \cdots, N_z. \tag{13}$$

The relaxation rate k_i was selected from a uniform probability density over the range $[\varepsilon, 1]$. The term $\zeta_i(t)$ is white Gaussian noise that satisfies $\langle \zeta_i(t) \rangle = 0$ and $\langle \zeta_i(t)\zeta_j(0) \rangle = 2M\delta_{ij}\delta(t)$. In this study, we set $\varepsilon = 0.0003$ and $N_z = 3000$, although change of these parameters has minor effects on the results described below, provided that ε is sufficiently small and N_z is sufficiently large.

The other parameter values were determined on the basis of experimental data given in Fig. 3 in the following manner. As observed in Fig. 3 *f*, two peaks appear in the histogram of IBIs for pattern *B*. The parameters τ, I, and d were determined so that the outputs of the model match the experimental data in terms of the position and the magnitude of each peak. The main influence of white noise, $\xi(t)$, was found to broaden the peaks in the histogram. Therefore, we determined the intensity of white noise, D, by matching the widths around the peaks in the histogram. By contrast, noise with long-term correlation, $z(t)$, controls the magnitude of the DFA fluctuation function, $F(n)$, in the scaling region of large n. Using this fact, we estimated the intensity of correlated noise, M. Finally, the parameter μ was determined so that the model can generate a profile of $F(n)$ similar to that obtained in the experiments. We found that this model successfully explains pattern *A* using the same parameter values except for μ. According to this procedure, the parameters were set as follows: $\tau = 0.7$, $I = 4.2$, $d = 0.06$, $x_{\text{th}} = 5$, $\sqrt{2D} = 0.07$, $\sqrt{2M} = 0.3$, and $\mu = 0.0182$ (pattern *A*) or 0.01 (pattern *B*).

We found that the abovementioned mathematical model successfully explains the experimental data in a semiquantitative manner. Fig. 7, *a* and *b*, display the raster plots, which were extracted from the time series of $x(t)$, when $\mu = 0.0182$ and $\mu = 0.01$, respectively. As can be clearly seen, a seemingly regular spike train, reminiscent of pattern *A*, is generated when $\mu = 0.0182$, while a burst pattern, reminiscent of pattern *B*, is obtained when $\mu = 0.01$. Fig. 7, *c*–*h*, displays the statistical properties of these temporal patterns: the time series of beat rates (Fig. 7, *c* and *d*), the histogram of IBIs (Fig. 7, *e* and *f*), and DFA (Fig. 7, *g* and *h*). Despite the fact that only a single parameter, μ, was changed, the model satisfactorily captures the essential features of the experimental data (Fig. 3), in terms of these statistical properties.

Fig. 8 displays the results of multifractal analysis of the time series of IBIs for this model using the WTMM method. By using the same parameter sets as those used in Fig. 7, the outputs of the model reasonably coincide with the experimental data with respect to the profiles of the partition functions (Fig. 7, *a* and *b*), the spectra of $\tau(q)$ (Fig. 7, *c* and *d*), and the spectra of $D(h)$ together with the positions of their maxima (Fig. 7, *e* and *f*).

DISCUSSION

In this study, several interesting characteristics were found in the spontaneous contractions of isolated single cardiac muscle cells. First, typical temporal patterns A and B were identified in the spontaneous contractions of single cells (Fig. 2, *a* and *b*). The temporal patterns of contraction varied from cell to cell under the same environmental conditions, and spontaneous transitions between these patterns were also found during a long experimental period (Fig. 2 *d*). By studying statistical properties of the time series of IBIs, the existence of $1/f^{\beta}$ noise ($\beta \approx 1$) at large timescales over 10^2 or 10^3 events was confirmed (see Figs. 3 and 4). Furthermore, the WTMM method applied to the IBI time series revealed multifractality at large timescales, i.e., the local Hölder exponents exhibited a broad spectrum at $\sim h \approx 0$ (Fig. 6). These characteristics were independent of the size of clusters, at least for small clusters that consist of a few cells. These experimental findings were reasonably explained by a modified Izhikevich model, in which white and long-term-correlated Gaussian noise was incorporated, in a semiquantitative manner (Figs. 7 and 8).

Fluctuations in the beat timings of cultured cardiac muscle cells have also been investigated in several earlier studies. Soen and Braun (10) and Yoneyama and Kawahara (11) studied fluctuations of single cardiac cells under similar experimental conditions to those of this study, and found power-law correlated fluctuations. However, in their studies, the presence of $1/f^{\beta}$ noise at large timescales was not addressed. Kucera et al. (9) performed a similar measurement on a monolayer of cultured muscle cells. They reported that in some cases, beat-rate fluctuations exhibit $1/f^{\beta}$ noise for frequencies <1 Hz. Since they studied a monolayer culture of cells in which a number of cells interacted with each other, it was not clear whether $1/f^{\beta}$ noise is an intrinsic property of each muscle cell or intercellular interactions are necessary to generate such noise. To address this question, we studied the statistical properties of single cells without interactions with other cells. Our experimental results indicate that $1/f^{\beta}$ noise is an intrinsic property of a single cardiac muscle cell. In addition, none of the earlier studies addressed the presence of multifractality at the single-cell level. In this study, multifractality was also identified at the single-cell level.

For mathematical examination, we introduced a stochastic integrate-and-fire model. The main features of the proposed model are the presence of a slow recovery variable y, which controls appearances of bursts, the presence of weak white Gaussian noise, and the presence of long-term correlated

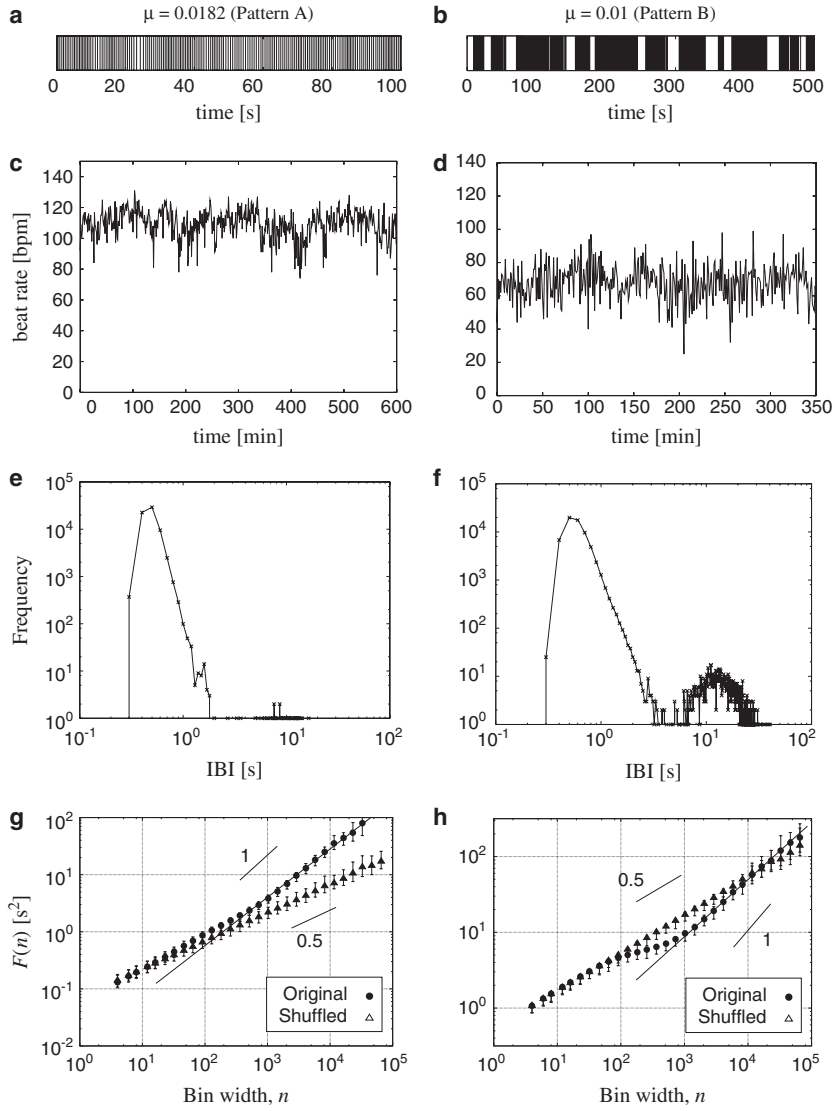

FIGURE 7 Statistical properties of the IBI time series generated by the mathematical model. The left columns (*a*, *c*, *e*, and *g*) represent the results obtained by setting $\mu = 0.0182$. The right columns (*b*, *d*, *f*, and *h*) display the results obtained by setting $\mu = 0.01$. (*a* and *b*) Raster plots of a portion of the time series. (*c* and *d*) Time series of the beat rate (number of beats per minute). (*e* and *f*) Histograms of the IBIs. (*g* and *h*) Detrended fluctuation analysis. The meanings of the symbols are the same as those in Fig. 3. The error bars in panels *g* and *h* represent the root mean-square deviations calculated from 20 independent runs. The solid lines are the least-squares fits to the original data in the range $[10^{2.5}, 10^{4.5}]$ in *g* and $[10^{3.2}, 10^{4.5}]$ in *h*, respectively. The scaling exponents α in these regions are 0.85 ± 0.01 in *g* and 0.75 ± 0.01 in *h*, respectively.

noise. Two kinds of noise, white noise and correlated noise, possess different roles in the behavior of the model. White noise increases the dispersion of IBIs and mainly contributes to the short-term fluctuations of IBIs. By contrast, correlated noise dominates the correlation of IBI fluctuations in the large timescales: The long-term correlation disappears in the absence of this noise. In this case, since the intensity of white noise was set small, the effects of correlated noise on the overall numerical results were much larger that those of white noise. Despite having only a small set of parameters, the model agrees extremely well with the experimental results. In our preliminary study, we found that other models, including ordinary differential equation models (33), can also reproduce the results, provided that the above-mentioned features are incorporated (not shown).

Possible molecular mechanism

The precise mechanism of $1/f^{\beta}$ noise present in the beat timings of single cardiac muscle cells is currently unclear, although a working hypothesis can be made on the basis of experimental findings of this study. As depicted in Fig. 2 *d*, spontaneous switching of patterns occurs at large timescales, even in a single cell. This implies that a variable that controls the appearance of patterns is fluctuating very slowly. We can speculate about a physical realization of this variable as follows. Firing patterns similar to the burst pattern observed in this study (pattern *B*) are already well known in pancreatic β-cells (34), various types of neurons (35), and embryonic-stem-cell-derived cardiac muscle cells (36). In these cases, adenosine-triphosphate (ATP)-dependent potassium current plays an important role in the occurrence of a burst activity (36–39). In this system (primary culture of neonatal ventricular muscle cells), we have confirmed that pattern *B* can be reversibly induced from pattern *A* by activating an ATP-dependent potassium channel (K_{ATP}). When sarcolemmal K_{ATP} of regularly beating cell (pattern *A*) was activated by adding several tens micromolar pinacidil, which is known as an activator of sarcolemmal K_{ATP} (40), to the culture

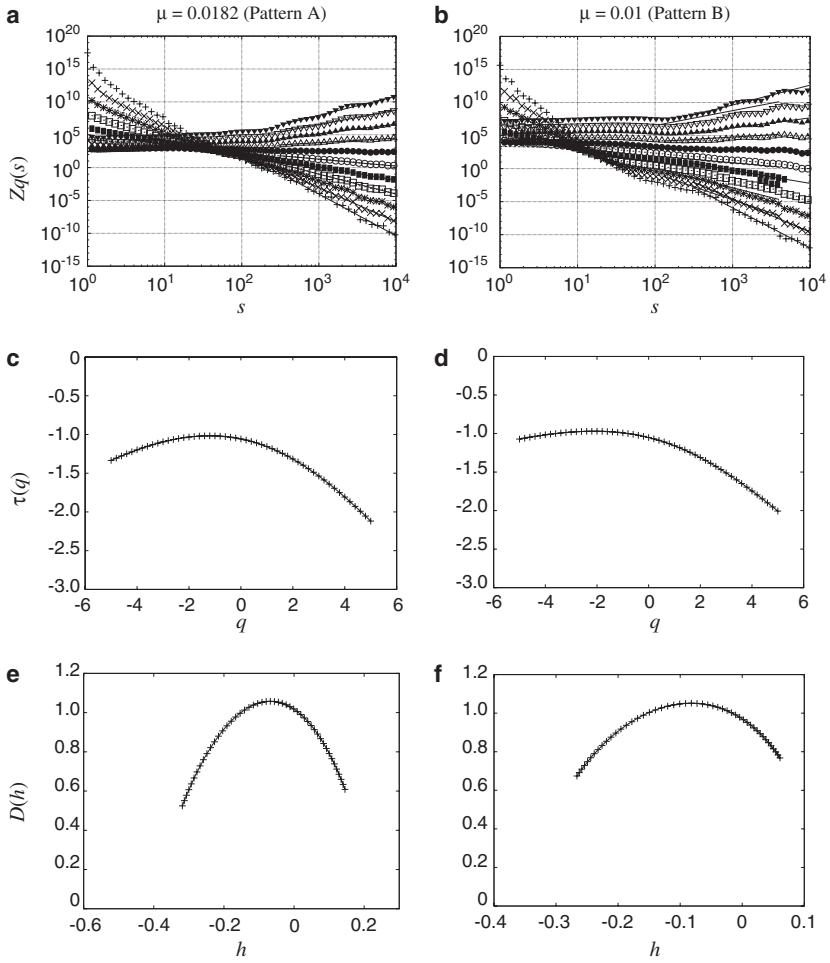

FIGURE 8 Multifractal analysis of the IBI time series generated by the mathematical model. The left columns (*a*, *c*, and *e*) represent data obtained by setting $\mu = 0.0182$, while the right columns (*b*, *d*, and *f*) represent data obtained by setting $\mu = 0.01$. (*a* and *b*) Partition functions, $Z_q(s)$, of integrated IBI time series. The meanings of the symbols are the same as those in Fig. 6. Thin solid lines are the least-squares fits to the data in the range $[10^{2.5}, 10^4]$. (*c* and *d*) The spectrum of the scaling exponent, $\tau(q)$, for the original IBI time series. (*e* and *f*) The spectrum of the local Hölder exponents, $D(h)$, for the original IBI time series.

medium, bursting activity similar to pattern *B* arose depending on the concentration of pinacidil, and pattern *A* resumes upon washout of pinacidil (T. Harada, unpublished data). This observation raises a possibility that the fluctuations in the intracellular ATP concentration causes the spontaneous switching between patterns *A* and *B*, and slow modulation in the metabolic state of the cell (41) might be a cause of slow modulation of the beat rate found in this study. To evaluate this hypothesis, however, requires much more examination of the role of such channels, the behavior over time of metabolic rates of a cell, and the correlation between the fluctuations of beat rates and metabolic rates.

Relation to heart rate variability

We noticed several differences between the characteristics of the fluctuations of beat timings at the single-cell level in vitro and those of heart-rate variability (HRV) observed in vivo. First of all, the burst pattern *B* does not appear in the heartbeats of healthy adults in vivo, although it was also observed in embryonic stem-cell-derived (36) and neonatal (10) cardiac muscle cells. Hence, the burst pattern in the spontaneous activity of cells is specific to in vitro systems of immature cells. This is possibly because of the difference in the intracellular ionic composition and the channel density (42,43).

In addition to the differences in temporal patterns, a difference in statistical properties was also found. In the earlier studies on the HRV using DFA, almost uniform scaling over extended timescales were observed for the heartbeat of healthy adult subjects (44). In contrast, at the cellular level, the presence of several distinct scaling regions and crossovers among them has been observed in this and earlier studies (5,9,10). Even in the apparently uniform pattern *A*, a crossover scaling was observed in DFA; fluctuations are uncorrelated at small timescales ($\alpha \approx 0.5$ for $n < 10^2$), and $1/f^{\beta}$ noise becomes significant at large timescales (see Fig. 3 *g*). A similar crossover scaling was observed in the results of numerical simulation of the mathematical model (Fig. 7). In the model studied here, one cause for the scaling exponent $\alpha \approx 0.5$ at small timescales is the presence of white noise. This is because this scaling region was found to shrink when the intensity of white noise, D, is decreased. However, it was found that the statistical properties of the model exhibit only slight changes when white noise was turned off, and that the crossover scaling was retained in the absence of white noise (not shown). Another reason for

the crossover scaling might be nonlinearity in the model, in particular that related to bursting behavior. As seen in Fig. 7 *h*, nonlinearity related to generation of bursting tends to suppress the correlation in IBI fluctuations at small and medium timescales, possibly because bursting interferes with correlated noise. This effect becomes evident when the parameters are set to induce pattern *B*, while the inherent nonlinearity might cause a similar effect when the parameter values are changed to induce pattern *A*. The outcomes of interactions between nonlinearity and noise in a bursting oscillator are to be studied in further detail.

In this study, we adopted ventricular cells derived from neonatal rats as a model system to study general features of the slow dynamics of membrane potential, because excitation of the membrane potential and contraction is coupled in this type of cell and because we are able to observe spontaneous contractions. Consequently, long-term correlation of the beat timings, which partly resembles the HRV, was found at the single-cell level, although several differences were also found as mentioned above. In addition, when we attempt to correlate the current experimental findings to the HRV, we have to be careful of the special nature of the experimental model adopted here. As is well known from the literature (42,43), ventricular cells derived from neonatal rats exhibit spontaneous contractions under physiological salt concentration, which this study also adopted. This feature does not appear in mature ventricular cells (43), and the autonomy is due to sinoatrial nodal cells in a healthy heart. Although the basic mechanisms of excitation and contraction are expected to be common to both neonatal ventricular cells and nodal cells, it is possible that these two types of cells have different characteristics in terms of long-term properties of fluctuations because of differences in system parameters, including the expression pattern of key proteins such as ion channels, signal transducing proteins, and motor proteins. Therefore, we have to extend this study to the case of sinoatrial nodal cells as a next step.

In addition to the cellular-level properties observed in this study, it is needless to state the importance of the contributions from other extracardiac control systems, including the autonomic nervous system, the hormonal system, and the pressure in the blood vessels, to the HRV in vivo (45). In particular, the autonomic nervous system is believed to be a key factor to generate the HRV (4,46,47). It is thus an interesting problem to examine the effect of external fluctuating input from neurons on the statistical properties of spontaneous activity of cells.

FUTURE PERSPECTIVES

In this study, the presence of $1/f^{\beta}$ noise and multifractality was established for the beat timings of single cardiac muscle cells. Further studies of the molecular mechanism generating such singular fluctuations should lead to insights into the mechanism maintaining the homeostasis of cellular activity at the single-cell level. In addition, it is also an important issue to study to what extent the properties observed in this case extend to other types of cells from various types of organisms, because this would reveal the general properties of fluctuations of cellular activities at large timescales.

T.H. and T.Y. gratefully acknowledge valuable support from Prof. K. Murase and Prof. H. Ikeda at the University of Fukui and Prof. K. Yoshikawa at Kyoto University.

This work was partly supported by grants from the Ministry of Education, Science, Sports, and Culture, Japan (No. 19031010), the Research and Education Program for Life Science at the University of Fukui, and the Asahi Glass Foundation.

REFERENCES

1. Goldberger, A. L., L. A. N. Amaral, J. M. Hausdorff, P. C. Ivanov, C. K. Peng, et al. 2002. Fractal dynamics in physiology: alternations with disease and aging. *Proc. Natl. Acad. Sci. USA*. 99:2466–2472.
2. Glass, L. 2001. Synchronization and rhythmic processes in physiology. *Nature*. 410:277–284.
3. Kobayashi, M., and T. Musha. 1982. 1/*f* fluctuation of heart rate period. *IEEE Trans. Biomed. Eng*. 29:456–457.
4. Kiyono, K., R. Struzik, N. Aoyagi, F. Togo, and Y. Yamamoto. 2005. Phase transition in a healthy human heart rate. *Phys. Rev. Lett*. 95: 058101.
5. Lowen, S. B., and M. C. Teich. 1996. The periodogram and Allan variance reveal fractal exponents greater than unity in auditory-nerve spike trains. *J. Acoust. Soc. Am*. 99:3585–3591.
6. Haussdorff, J. M., C. K. Peng, Z. Ladin, J. Y. Wei, and A. L. Golberger. 1995. Is walking a random walk? Evidence for long-range correlations in stride interval of human gait. *J. Appl. Physiol*. 78:349–358.
7. Duarte, M., and V. M. Zatsiorsky. 2001. Long-range correlations in human standing. *Phys. Lett. A*. 283:124–128.
8. Zbilut, J. P., G. Mayer-Kress, P. A. Sobotka, M. O'Toole, and J. J. X. Thomas. 1989. Bifurcations and intrinsic chaotic and 1/*f* dynamics in an isolated perfused rat heart. *Biol. Cybern*. 61:371–378.
9. Kucera, J. P., M. O. Heuschkel, P. Renaud, and S. Rohr. 2000. Power-law behavior of beat-rate variability in monolayer cultures of neonatal rat ventricular myocytes. *Circ. Res*. 86:1140–1145.
10. Soen, Y., and E. Braun. 2000. Scale-invariant fluctuations at different levels of organization in developing heart cell networks. *Phys. Rev. E Stat. Phys. Plasmas Fluids Relat. Interdiscip. Topics*. 61: R2216–R2219.
11. Yoneyama, M., and K. Kawahara. 2004. Coupled oscillator systems of cultured cardiac myocytes: Fluctuation and scaling properties. *Phys. Rev. E Stat. Nonlin. Soft Matter Phys*. 70:021904.
12. Lowen, S. B., S. S. Cash, M. -M. Poo, and M. C. Teich. 1997. Quantal neurotransmitter secretion rate exhibits fractal behavior. *J. Neurosci*. 17:5666–5677.
13. Bucher, O. M. 1957. A photoelectric recording set for pulsation curves of heart muscle cultures in vitro. *Exp. Cell Res*. 13:109–115.
14. Rohr, S. 1990. A computerized device for long-term measurements of the contraction frequency of cultured rat heart cells under stable incubating conditions. *Pflugers Arch*. 416:201–206.
15. Soen, Y., N. Cohen, D. Lipson, and E. Braun. 1999. Emergence of spontaneous rhythm disorders in self-assembled networks of heart cells. *Phys. Rev. Lett*. 82:3556–3559.
16. Katz, A. M. 2005. Physiology of the Heart, 4th Ed. Lippincott Williams & Wilkins, Philadelphia, PA.
17. Peng, C. -K., J. Mietus, J. M. Hausdorff, S. Havlin, H. E. Stanley, et al. 1993. Long-range anticorrelations and non-Gaussian behavior of the heartbeat. *Phys. Rev. Lett*. 70:1343–1346.

18. Ivanov, P. C., L. A. N. Amaral, A. L. Goldberger, S. Havlin, M. G. Rosenblum, et al. 1999. Multifractality in human heartbeat dynamics. *Nature*. 399:461–465.

19. Izhikevich, E. M. 2006. Dynamical Systems in Neuroscience: The Geometry of Excitability And Bursting. MIT Press, Cambridge, MA.

20. Harada, T., and A. Isomura. 2006. Spontaneous formation of cell clusters in a cardiac cell culture system. *Prog. Theor. Phys.* 161:107–118.

21. Harada, T., A. Isomura, and K. Yoshikawa. 2008. Contraction-induced cluster formation in cardiac cell culture. *Physica D. In press.*

22. Lokuta, A., M. S. Kirby, S. T. Gaa, W. J. Lederer, and T. B. Rogers. 1994. On establishing primary cultures of neonatal rat ventricular myocytes for analysis over long periods. *J. Cardiovasc. Electrophysiol.* 5:50–62.

23. Peng, C. K., S. V. Buldyrev, S. Havlin, M. Simons, H. E. Stanley, et al. 1994. Mosaic organization of DNA nucleotides. *Phys. Rev. E Stat. Phys. Plasmas Fluids Relat. Interdiscip. Topics.* 49:1685–1689.

24. Muzy, J. F., E. Bacry, and A. Arneodo. 1993. Multifractal formalism for fractal signals: the structure-function approach versus the wavelet-transform modulus-maxima method. *Phys. Rev. E Stat. Phys. Plasmas Fluids Relat. Interdiscip. Topics.* 47:875–884.

25. Hansel, D., G. Mato, C. Meunier, and L. Neltner. 1998. On numerical simulations of integrate-and-fire neural networks. *Neural Comput.* 10:467–483.

26. Kort, A. A., M. C. Capogrossi, and E. G. Lakatta. 1985. Frequency, amplitude, and propagation velocity of spontaneous Ca^{++} dependent contractile waves in intact adult rat cardiac muscle and isolated myocytes. *Circ. Res.* 57:844–855.

27. Bertram, R., M. J. Butte, T. Kiemel, and A. Sherman. 1995. Topological and phenomenological classification of bursting oscillations. *Bull. Math. Biol.* 57:413–439.

28. Bub, G., L. Glass, N. G. Publicover, and A. Sherier. 1998. Bursting calcium rotors in cultured cardiac myocytes monolayers. *Proc. Natl. Acad. Sci. USA.* 95:10283–10287.

29. Bub, G., A. Sherier, and L. lass. 2005. Global organization of dynamics in oscillatory heterogeneous excitable media. *Phys. Rev. Lett.* 94: 028105.

30. Parisi, G., and U. Frisch. 1985. Proceedings of the International School on Turbulence and Predictability in Geophysical Fluid Dynamics and Climate Dynamics. M. Ghil, R. Benzi, and G. Parisi, editors. North-Holland, Amsterdam, The Netherlands.

31. Muzy, J. F., E. Bacry, and A. Arneodo. 1991. Wavelets and multifractal formalism for singular signals: application to turbulence data. *Phys. Rev. Lett.* 67:3515–3518.

32. Lin, D. C., and R. L. Hughson. 2001. Modeling heart rate variability in healthy humans: a turbulence analogy. *Phys. Rev. Lett.* 86:1650–1653.

33. Hindmarsh, J. L., and R. M. Rose. 1984. A model of neuronal bursting using three coupled first order differential equations. *Proc. R. Soc. Lond. B. Biol. Sci.* 221:87–102.

34. Lebrun, P., and I. Atwater. 1985. Chaotic and irregular bursting electrical activity in mouse pancreatic B-cells. *Biophys. J.* 48:529–531.

35. Wang, X. J., and J. Rinzel. 1995. Oscillatory and bursting properties of neurons. *In* The Handbook of Brain Theory and Neural Networks. M. Arbib, editor. MIT Press, Cambridge, MA.

36. Gryshchenko, O., I. R. Fischer, M. Dittrich, S. Viatchenko-Karpinski, J. Soest, et al. 1999. Role of ATP-dependent K^+ channels in the electrical excitability of early embryonic stem cell-derived cardiomyocytes. *J. Cell Sci.* 112:2903–2912.

37. Smolen, P., and J. Keizer. 1992. Slow voltage inactivation of Ca^{2+} currents and bursting mechanisms for the mouse pancreatic β-cell. *J. Membr. Biol.* 127:9–19.

38. Kinard, T. A., G. de Vries, A. Sherman, and L. S. Satin. 1999. Modulation of the bursting properties of single mouse pancreatic β-cells by artificial conductances. *Biophys. J.* 76:1423–1435.

39. de Vries, G., and A. Sherman. 2000. Channel sharing in pancreatic β-cells revisited: enhancement of emergent bursting by noise. *J. Theor. Biol.* 207:513–530.

40. Seino, S., and T. Miki. 2003. Physiological and pathophysiological roles of ATP-sensitive K^+ channels. *Prog. Biophys. Mol. Biol.* 81:133–176.

41. Rourke, O., B. M. Ramza, and E. Marban. 1994. Oscillations of membrane current and excitability driven by metabolic oscillations in heart cells. *Science.* 265:962–966.

42. Miake, J., E. Marbán, and H. B. Nuss. 2002. Biological pacemaker created by gene transfer. *Nature.* 419:132–133.

43. de Boer, T. P., M. A. G. van der Heyden, M. B. Rook, R. Wilders, R. Broekstra, et al. 2006. Pro-arrhythmogenic potential of immature cardiomyocytes is triggered by low coupling and cluster size. *Cardiovasc. Res.* 71:704–714.

44. Viswanathan, G. M., C. K. Peng, H. E. Stanley, and A. L. Golberger. 1997. Deviations from uniform power law scaling in nonstationary time series. *Phys. Rev. E Stat. Phys. Plasmas Fluids Relat. Interdiscip. Topics.* 55:845–849.

45. Kotani, K., Z. R. Struzik, K. Takamasu, H. E. Stanley, and Y. Yamamoto. 2005. Model for complex heart rate dynamics in health and diseases. *Phys. Rev. E Stat. Nonlin. Soft Matter Phys.* 72:041904.

46. Bunde, A., S. Havlin, J. W. Kantelhardt, T. Penzel, J. -H. Peter, et al. 2000. Correlated and uncorrelated regions in heart-rate fluctuations during sleep. *Phys. Rev. Lett.* 85:3736–3739.

47. Osaka, M., H. Kumagai, K. Sakata, T. Onami, K. H. Chon, et al. 2003. Low-order chaos in sympathetic nerve activity and scaling of heartbeat intervals. *Phys. Rev. E Stat. Nonlin. Soft Matter Phys.* 67:041915.